JOURNAL OF SOLID STATE CHEMISTRY 90, 109–125 (1991)

On the Pr_nO_{2n-2} Series of Oxides and the Structure of $Pr_{24}O_{44}$: An Investigation by High-Resolution Electron Microscopy

E. SCHWEDA,* D. J. M. BEVAN,† AND L. EYRING

Department of Chemistry and Center for Solid State Science, Arizona State University, Tempe, Arizona 85287-1604

Received February 22, 1988; in revised form September 12, 1990

The ordered intermediate rare earth oxides of praseodymium in the composition range between $PrO_{1.714}$ and $PrO_{1.833}$ (Pr_nO_{2n-2}, n = 7, 9, 10, 11, 12) are easily transformed into each other by the variation of temperature and/or oxygen pressure. X-ray powder diffraction patterns of all the intermediate phases are fluorite-related and it is supposed that there are structural relationships between members of the homologous series. Group–subgroup relationships are discussed within this framework, and the probable structure of $Pr_{24}O_{44}$ is proposed. The unit cell, reported as monoclinic from electron diffraction studies, is assumed to contain two clusters, each with contents Pr_7O_{30}, but no definitive structure analysis has been made. From the contrast variation observed in a high-resolution electron microscope (HREM) image of $Pr_{24}O_{44}$ the relative positions and orientation of these clusters can be inferred, which allows selection of a unique model from those possible. This same image further suggests that the unit cell is actually triclinic. The atomic coordinates have been calculated for the two defect clusters within the unit cell, and have been used for image calculations and simulation comparisons.

Introduction

At compositions between the C-type sesquioxide, Pr_2O_3, and the fluorite-type dioxide, PrO_2, the existence of ordered intermediate phases of the homologous series Pr_nO_{2n-2} (n = 7, 9, 10, 11, 12) has been well established (*1*); unit cells for these have been determined by electron diffraction (ED) and high-resolution electron microscopy (HREM) (*2*). All have structures related to fluorite-type PrO_2 (space group $Fm\bar{3}m$) and maintain a f.c.c. arrangement of metal atoms (the only phase of this group of related oxides for which the structure has been reported is the n = 7 member of the series) (*3, 4*). The complete determination of the structures of the ordered, intermediate binary oxides of the rare earths is an extremely difficult problem which will require some improvement in equipment and techniques to solve. However, techniques and methods presently available can be and have been used to advance our understanding of these structures. What follows is a modeling approach, allied with the results of electron diffraction/microscopy, which offers some insights into the general structural pattern of this homologous series of oxides. In particular we consider in detail several struc-

* Present address: Universität Tübingen Institut für Anorganische Chemie, Auf der Morgenstelle 18, D-7400 Tübingen, FRG.

† School of Physical Sciences, Flinders University of South Australia, Bedford Park, South Australia 5042.

0022-4596/91 $3.00

tural possibilities for the member $n = 12$, the well-known Pr_6O_{11} phase.

Structural Considerations of Defects in Binary Rare-Earth Oxides

According to classical (Schottky–Wagner) defect theory, the defects in the fluorite-related, binary rare-earth oxides would be isolated anion vacancies, which may indeed be present at compositions very close to PrO_2 and at each ordered, intermediate phase. However, all the structural evidence available for these and related compounds with O/M significantly less than 2.00 suggests strongly that "vacancies" occur in pairs across the body diagonal to the MO_8 fluorite-type cube, i.e., separated by $\frac{1}{2}\langle 111\rangle_F$. The absence of anions on these sites, which are tetrahedrally coordinated by metal atoms, gives rise to a relaxation from their strictly f.c.c. sites of the six peripheral metal atoms which lie in the immediate vicinity of the vacancies around this $\langle 111\rangle_F$ direction. This extended defect M_7O_{30} now involves seven cations, a central 6-coordinated one (squashed octahedron) surrounded by six 7-coordinated cations, three above and three below as viewed along the axis of the "vacancy pair." The point-group symmetry of this now-distorted element of the original fluorite-type structure is reduced to $\bar{3}2/m$. This same cluster was the basis for the structure proposed by Baenziger *et al.* (*3*) for Tb_7O_{12}. Its possible role in anion-deficient, fluorite-related superstructures was later elaborated by Hyde and Eyring (*5*) and its occurrence as a single entity was revealed in the structure of $Zr_{10}Sc_4O_{26}$ (*6*). The M_7O_{12} structure, e.g., UY_6O_{12} (*7*) has been described as consisting only of these units sharing edges to fill space. In this work we adopt the view that this M_7O_{30} cluster is the basic building block for all the known intermediate praseodymium oxides, and explore how these clusters can link together to form various model structures.

All the homologues of the intermediate praseodymium oxides appear to have at least one unit-cell axis in common, viz. $\frac{1}{2}\langle 211\rangle_F$, so this projection has been commonly used to describe what is already known about their structures; however, it requires some explanation. Figs. 1a and 1b show the $\frac{1}{2}[21\bar{1}]_F$ projection, which is one (chosen arbitrarily) of the 24 possible for a face-centered-cubic cell (i.e., 12 pairs related by centrosymmetry). Superimposed on this is the fluorite unit cell, drawn as a right-handed system, and the small cube shows the anion coordination of a metal atom in fluorite, with a vacancy pair along $\frac{1}{2}[111]_F$ indicated by filled circles. For the unit cells of the intermediate praseodymium oxide phases, none of which is orthogonal, this $\frac{1}{2}[21\bar{1}]_F$ fluorite vector, taken as the a-axis is not perpendicular to the bc-planes, but is perpendicular to the plane of projection, which is the reference plane of height zero. The heights of all projected atoms and lattice points of the idealized structures are then expressed as fractions of the $\frac{1}{2}[21\bar{1}]_F$ vector above or below this projection plane. These heights will not, of course, correspond to the x-coordinates of the atoms in actual unit cells.

Figure 2a shows the ideal M_7O_{30} defect cluster, with the vacancy pair along $[111]_F$, in the $\frac{1}{2}[21\bar{1}]_F$ $(=[100]_7)$ projection. Figure 2b is a stereoscopic view of this ideal cluster. Figure 3 shows, in a stereoscopic view down $\frac{1}{2}[21\bar{1}]_F$, the actual cluster occurring in Pr_7O_{12} (*4*). Assuming that other phases between Pr_7O_{12} and PrO_2 in the praseodymium–oxygen system incorporate the same kind of defect, their structures should be related.

Structural Relationship between Binary Rare-Earth Oxides

The theory of symmetry changes at continuous phase transitions predicts that the symmetry group of the low-temperature

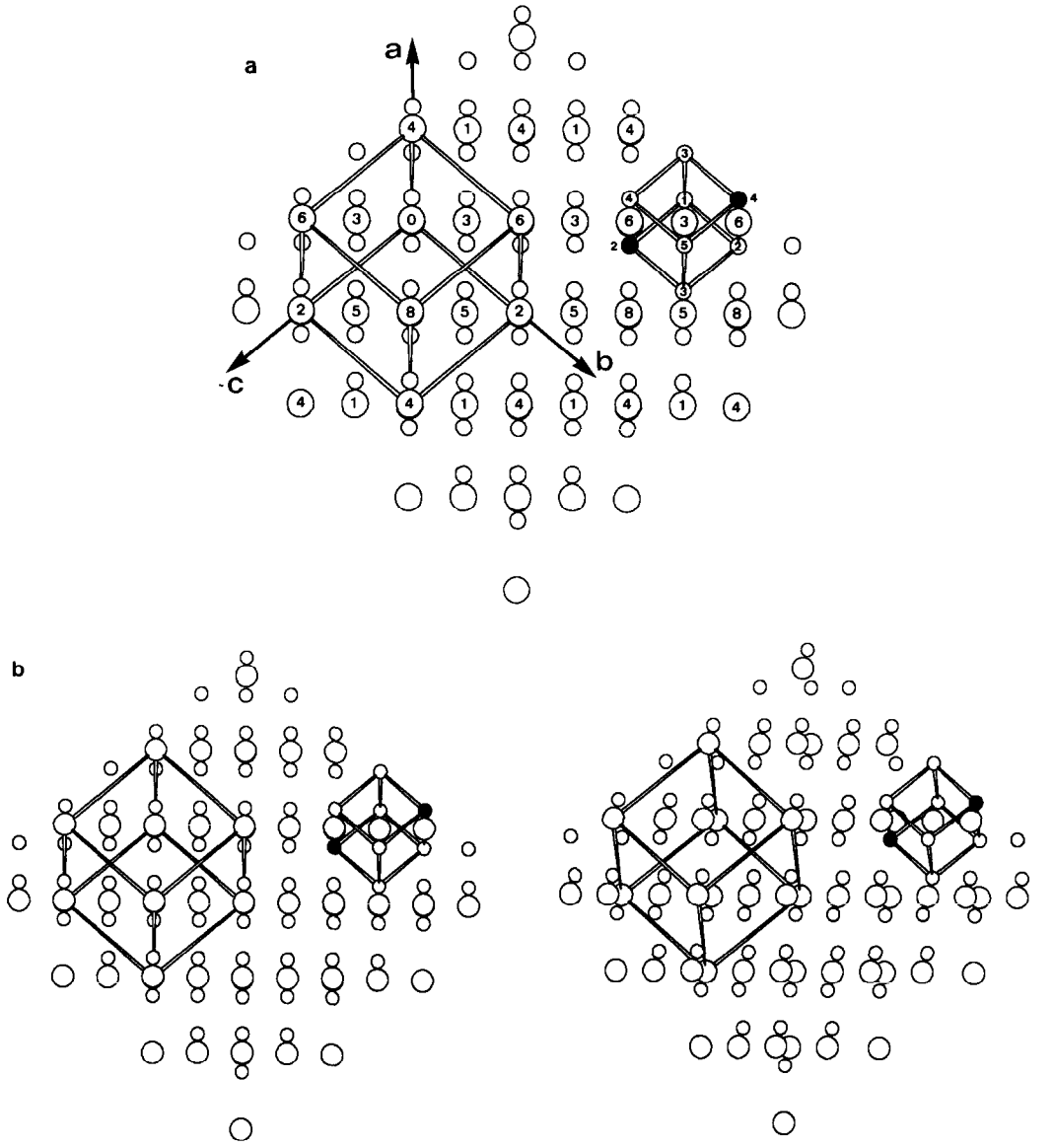

FIG. 1. The fluorite structure: (a) The $\frac{1}{2}[21\bar{1}]_F$ projection of rows of atoms in the fluorite structure. (b) A stereographic view along $\frac{1}{2}[21\bar{1}]_F$. In both cases a fluorite unit cell and the MX_8 cube are shown. Large open circles represent metal atoms; small open circles represent nonmetal atoms. Heights are expressed as sixths of $\frac{1}{2}[21\bar{1}]_F$. The vacancy pair across $\frac{1}{2}[111]_F$ is indicated by filled small circles.

phase is a subgroup of that for the high-temperature phase (*8*). Bernal first applied this principle to topotactical reactions involving only small relative changes of the atomic positions (*9*). In this same context, Boulesteix and Eyring (*10*) have demonstrated that well-defined epitaxial growth of one phase on another during reduction of thin films of Pr_9O_{16} to Pr_7O_{12} is primarily responsible for providing reconstructive

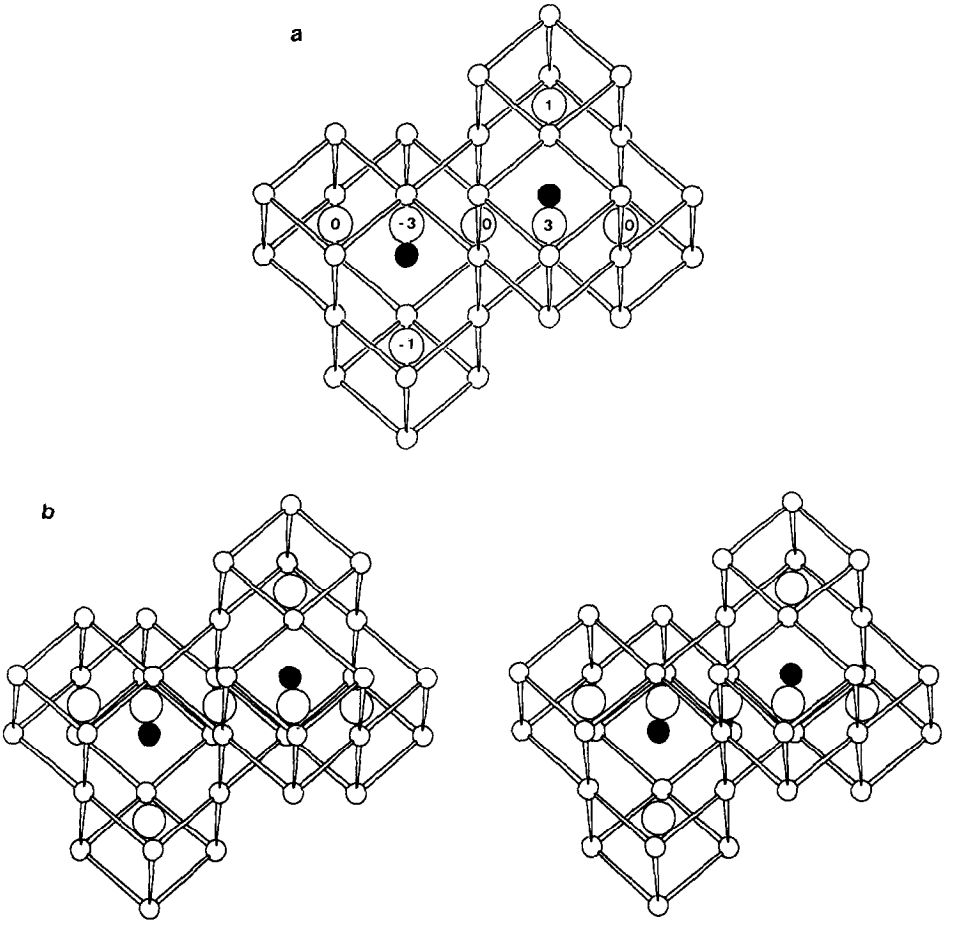

FIG. 2. The isolated M_7O_{30} cluster: (a) Projected down $\frac{1}{2}[21\bar{1}]_F$. (b) A stereoscopic view along $[100]_7 = \frac{1}{2}[21\bar{1}]_F$.

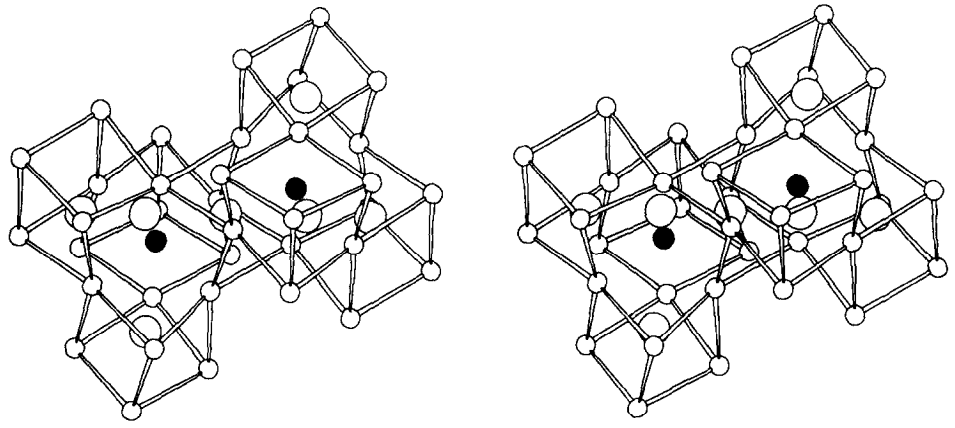

FIG. 3. A stereoscopic view along $[100]_7 = \frac{1}{2}[21\bar{1}]_F$ of the actual cluster present in the structure of Pr_7O_{12}. Vacancies are shown as filled small circles.

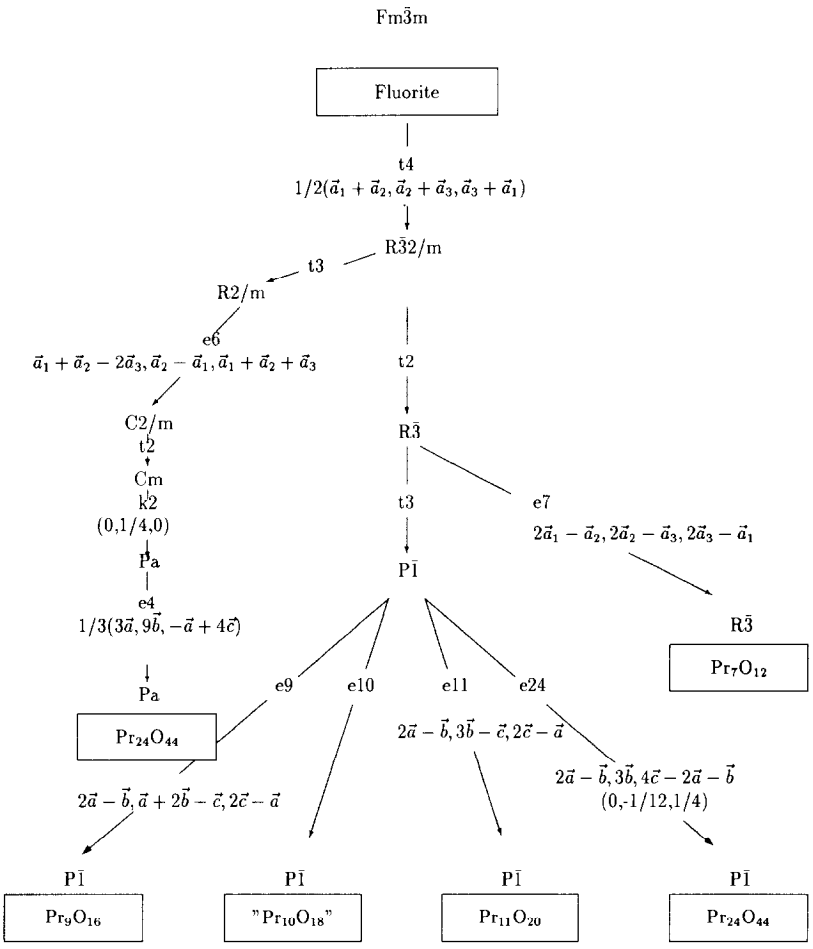

FIG. 4. Group–subgroup relationships for the praseodymium oxides.

change with many of the characteristics of a diffusionless transformation, and this seems to be generally true for all reactions between the intermediate binary rare-earth oxides. It is the integrity, in essence, of the fluorite-type, f.c.c cation lattice (albeit with slight distortions) over the whole composition range that constitutes the essential basis for topotaxy, so that the structural changes occurring during oxidation or reduction (both very facile) can be described simply as rearrangements of M_7O_{30} defect clusters, and these, we assert, must take place within the constraints imposed by the group–subgroup relationships stemming from the aristotype structure, RO_2. These relationships are shown in Fig. 4 for the known intermediate praseodymium oxides, and include a branch leading to possible monoclinic cells. We shall return to this later.

We begin our modeling studies with the known structure of Pr_7O_{12} (*4*) (assumed to be isostructural with UY_6O_{12} (*7*)). The unit cell is rhombohedral (space group $R\bar{3}$) and is related to the fluorite cell as follows:

$$a_7 = a_F + \tfrac{1}{2}b_F - \tfrac{1}{2}c_F,$$

$$b_7 = -\tfrac{1}{2}a_F + b_F + \tfrac{1}{2}c_F,$$

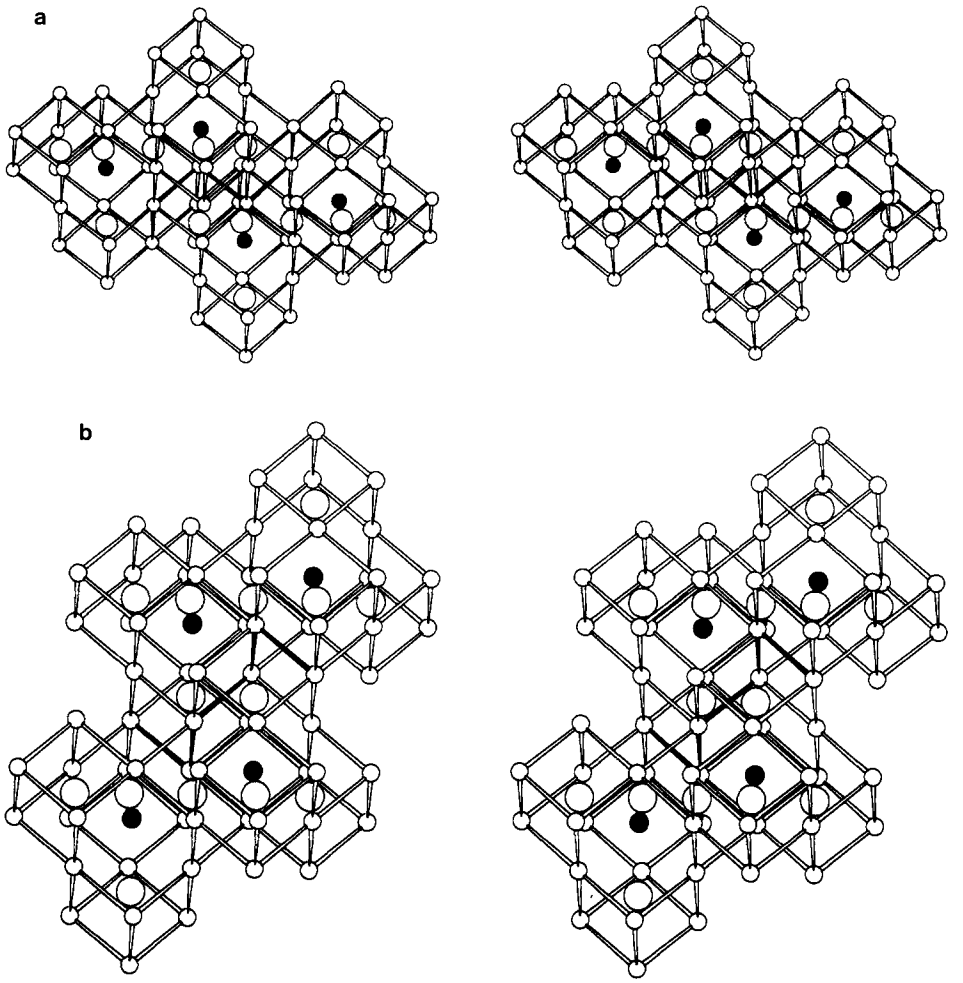

FIG. 5. The M_7O_{12} structure: (a) A stereoscopic view along $[100]_7 = \frac{1}{2}[21\bar{1}]_F$ of the cluster linkage along $[010]_7 = \frac{1}{2}[\bar{1}21]_F$. (b) A stereoscopic view along $[100]_7 = \frac{1}{2}[1\bar{1}2]_F$. Filled small circles indicate vacancies, cluster centers are between vacancies, and cluster junctions are highlighted.

$$c_7 = \tfrac{1}{2}a_F - \tfrac{1}{2}b_F + c_F.$$

The vacancy pair lies on the threefold axis, which is $[111]_F$ so that the angle between this and the $\frac{1}{2}\langle 211\rangle_F$ cell translations is 61.87°. Figures 5a and 5b show the cluster connectivities (always edge-sharing to preserve the f.c.c. cation array), viewed stereoscopically down the a_7 axis $(\frac{1}{2}[21\bar{1}]_F$. These connectivities are unambiguous in this structure, and represent the densest possible cluster packing, but for other members of the homologous series the situation is not so clear. For the odd members $n = 9$ (Pr_9O_{16}) and 11 ($Tb_{11}O_{20}$) the respective triclinic unit cells contain just one cluster, and two of the translations seem to be the same as for the Pr_7O_{12} cell, viz.,

$$a_9 = a_F + \tfrac{1}{2}b_F - \tfrac{1}{2}c_F,$$

$$c_9 = \tfrac{1}{2}a_F - \tfrac{1}{2}b_F + c_F.$$

The b-axes are respectively $b_9 = \frac{1}{2}[031]_F$ and $b_{11} = \frac{1}{2}[\bar{1}32]_F$ on this basis (*2*). In these tri-

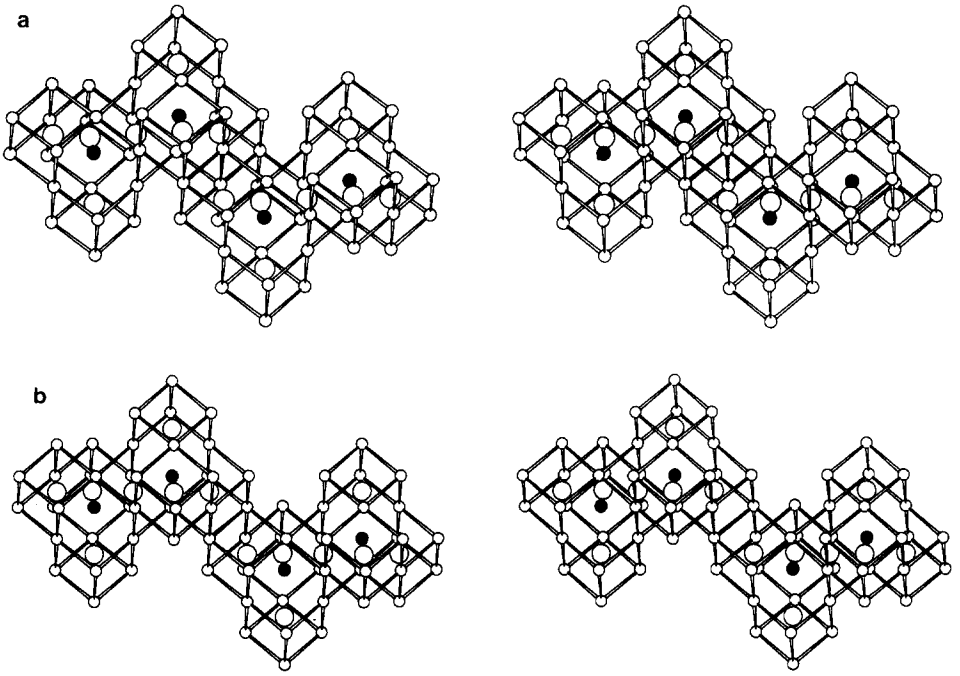

FIG. 6. The proposed M_9O_{16} and $M_{11}O_{20}$ structures: (a) A stereoscopic view along $[100]_9 = \frac{1}{2}[21\bar{1}]_F$ of the cluster linkage along $[001]_9 = \frac{1}{2}[031]_F$. (b) A stereoscopic view along $[100]_{11} = \frac{1}{2}[21\bar{1}]_F$ of the cluster linkage along $[010]_{11} = \frac{1}{2}[\bar{1}32]_F$. In both cases the linkage along $[001]_n$ is taken as that shown in Fig. 5b. Filled small circles indicate vacancies, cluster centers are between vacancies, and cluster junctions are highlighted.

clinic cells there are no symmetry factors that might fix the orientation of the vacancy pair with the *a*- and *c*-axes respectively, as in Pr_7O_{12}, but we have assumed no change from the angle of 61.87° and have shown in Figs. 6a and 6b the connectivities of clusters along the *b*-axes of these cells, while accepting the connectivities along the *a*- and *c*-axes to be the same as those depicted for Pr_7O_{12} in Fig. 5. However, other possibilities must be considered.

As a starting point we fix the orientation of the vacancy pair in the basic M_7O_{30} cluster to be along $[111]_F$. There are now four distinguishable $\frac{1}{2}\langle 211\rangle_F$, center-to-center cluster linkages for which the angles between the unique $[111]_F$ and $\langle 211\rangle_F$ are, respectively, 19.47, 61.87, and 90.0°. The first can be excluded from consideration since for this the vacancy pairs approach each other too closely ($\frac{1}{2}\langle 100\rangle_F$); the second orientation is the one present in Pr_7O_{12}; the third has not previously been considered but is a viable alternative. For Pr_9O_{16}, it is possible to choose more than one cell consistent with the electron diffraction evidence, for which the $\frac{1}{2}\langle 211\rangle_F$ cluster linkages are of different kinds, viz.,

$a_9 = \frac{1}{2}[11\bar{2}]_F$: angle with $[111]_F$ is 90.0°,

$b_9 = \frac{1}{2}[031]_F$,

$c_9 = \frac{1}{2}[2\bar{1}1]_F$: angle with $[111]_F$ is 61.87°.

This cell has only slightly different angles from those of the Kunzmann/Eyring cell (*2*); the values, with those for the latter cell in square brackets, are $\alpha = 105°$ [97°], $\beta = 99.6°$ [99.6°], $\gamma = 82.6°$ [75°]. Another such cell, however, has very different values for the angles α and γ and is not considered

further. It should be mentioned in passing that powder X-ray diffraction indicates a high- and low-temperature form of Pr_9O_{16} (*11*). The same is true for the analogous $Tb_{11}O_{20}$ ($Pr_{11}O_{20}$ has a different unit cell). An alternative cell is:

$a_{11} = \frac{1}{2}[2\bar{1}1]_F$: angle with $[111]_F$ is 61.87°,

$b_{11} = \frac{1}{2}[123]_F$,

$c_{11} = \frac{1}{2}[1\bar{2}1]_F$: angle with $[111]_F$ is 90.0°.

For this cell, the angle γ (83.7°) is the supplement of that for the Kunzmann/Eyring cell (96.3°), while the others are identical.

We can also produce primitive cells for the homologues $n = 10$ and $n = 12$, but electron diffraction and high-resolution imaging show that there are four formula units per cell for the former and two for the latter; both have been reported as having monoclinic symmetry. We now focus attention on the structure of $Pr_{24}O_{44}$ (the so-called $\beta(1)$ phase).

On the Structure of $Pr_{24}O_{44}$

The unit cell of $\beta(1)$ as determined by electron and X-ray diffraction has cell parameters as follows: $a = 6.687$, $b = 11.602$, $c = 12.829$, $\alpha = 90°$, $\beta = 100.7°$, $\gamma = 90°$. Single-crystal X-ray analysis and the results of electron diffraction (*12, 13*) indicate a monoclinic space group Pc, $P2/c$ or $P2_1/c$. However, there is some uncertainty about the true space group, and in previous work involving the interpretation of HREM images, the triclinic group $P\bar{1}$ was proposed (*13*). The relationship of the β cell to that of fluorite is given below:

$$a_\beta = a_F + \tfrac{1}{2}b_F - \tfrac{1}{2}c_F$$

$$b_\beta = \tfrac{3}{2}b_F + \tfrac{3}{2}c_F$$

$$c_\beta = a_F - \tfrac{3}{2}b_F + \tfrac{3}{2}c_F.$$

In our description, this cell must contain two of the M_7O_{30} clusters, the "molecules of the structure" so to speak. So far, in all the models discussed the clusters have been congruent, but it is unusual to have two such entities unrelated in a cell with $P\bar{1}$ symmetry. It is much more likely that the two clusters of the β cell are enantiomorphs, related either by a center of symmetry or a glide reflection, the latter giving rise to the monoclinic cell, as reported, and the former to a triclinic cell with $P\bar{1}$ symmetry.

There are, of course, numerous possibilities for arranging clusters in this unit cell, although these are limited if we consider only those arrangements in which there is no overlap of cluster cations, i.e., one or more such cations common to two clusters, and also reject those which result in vacancies from neighboring clusters being too closely juxtaposed, e.g., along $\frac{1}{2}\langle 110\rangle_F$ or $\frac{1}{2}\langle 100\rangle_F$. Moreover, in deriving such models, the constraints of the group–subgroup relationships must apply, and the choice of origin assumes considerable importance. For example, the $P\bar{1}$ cell of $Pr_{24}O_{44}$ is derived from a primitive $P\bar{1}$ basis cell (see Fig. 4) by enlarging the latter 24 times and only retaining the inversion points of the expanded cell, which will, of course, be from the set of the basis cell. This basis cell itself derives from the primitive $R\bar{3}$ cell, and there are various choices of origin for the basis cell, and therefore the $\beta(1)$ cell, in relation to the nominally invariant fluorite cations. Likewise, if the Pa monoclinic cell obtains, its glide-reflection planes must be normal to the unique b-axis and be part of the set of glide-reflection planes of the supergroup $R\bar{3}2/m$. This requirement gives rise to the condition that the vacancy pair axis (taken as $[111]_F$) be parallel to the glide-reflection planes and therefore at right angles to the monoclinic b-axis.

Models with an Angle of 90° between $a_\beta = \frac{1}{2}\langle 211\rangle_F$ and the $[111]_F$ Vacancy Orientation

For monoclinic models the vacancy pair axis ($[111]_F$) is normal to b, so that b must have the form $\langle\bar{3}03\rangle_F$; such a cell could be

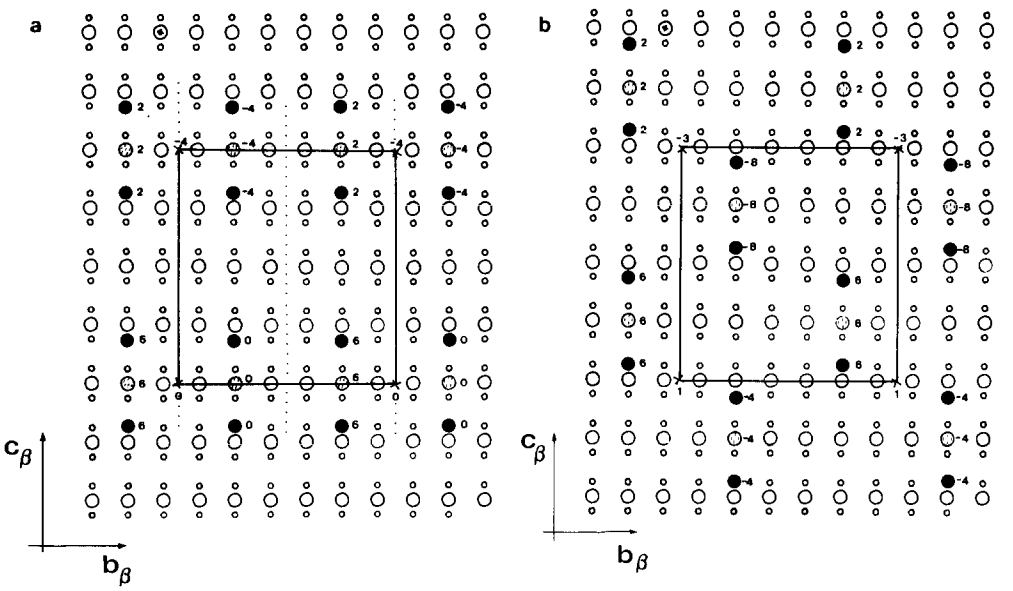

FIG. 7. Structural models for the alternative cell of $Pr_{24}O_{44}$ in which the vacancy pair axis is at right angles to the $\frac{1}{2}\langle\bar{1}2\bar{1}\rangle$ projection axis. (a) Idealized projection down $[100]_\beta = \frac{1}{2}[\bar{1}2\bar{1}]_F$ of the model for the *Pa* structure of $Pr_{24}O_{44}$. (b) Idealized projection down $[100]_\beta = \frac{1}{2}[\bar{1}2\bar{1}]_F$ of the model for the $P\bar{1}$ structure of $Pr_{24}O_{44}$. Cluster centers are shown as large, hatched circles and vacancies as filled intermediate circles. Heights are expressed as twelfths of $\frac{1}{2}[\bar{1}2\bar{1}]_F$.

$a_\beta = \frac{1}{2}[\bar{1}2\bar{1}]_F$ (angle with $[111]_F$ is 90°),

$b_\beta = \frac{1}{2}[\bar{3}03]_F$,

$c_\beta = \frac{1}{2}[323]_F$ ($\alpha = \gamma = 90°; \beta = 100°$).

This is qualitatively different from those cells in which the angle between the $[111]_F$ vacancy pair axis and a_β is 61.87° and Fig. 7a shows what we believe to be the only allowed model (in accordance with the imposed constraints) in space group *Pa*. Figure 7b shows yet another model for this cell in space group $P\bar{1}$; again, we believe it to be the only one allowed.

Some years ago a *Pm* model of this cell was also considered by Summerville *et al.* (*13*), but this is not allowed under group–subgroup relationships.

Models with an Angle of 61.87° between $a_\beta = \frac{1}{2}\langle 211\rangle_F$ and the $[111]_F$ Vacancy Orientation

In exploring triclinic models, we have assumed that the *a*-axis of $\beta(1)$ is the same as in Pr_7O_{12}, i.e., $\frac{1}{2}[21\bar{1}]_F$, making an angle of 61.87° with the $[111]_F$ axis of the vacancy pair. Those models in $P\bar{1}$ which turned out to be viable within this framework are summarized in Table I; in each case the unit cell has the same relationship, already quoted, to the fluorite parent, and the choice of origin on an inversion center is described. In the absence of a full structural analysis, selection of a likely model can only be made on the basis of the experimental evidence available, and this has come mainly from HREM. Figure 8 shows such an image, with the unit cell marked to emphasize the clearly visible superstructure. The evidence from this is that the clusters are shifted relative to one another in projection by the vector 0, $\frac{1}{6}$, $\frac{1}{2}$ (or 0, $-\frac{1}{6}$, $\frac{1}{2}$) of the $\beta(1)$ cell. This points to model 4, which is shown in Figs. 8 and 9 and further suggests that the orientation of the vacancy pairs (black contrast) also seems to correspond with this model. A similar HREM image has already been reported by Summerville *et al.* (*13*). Thus

TABLE I

POSSIBLE CLUSTER ARRANGEMENTS IN THE UNIT CELL OF $Pr_{24}O_{44}$, PROJECTED DOWN $\frac{1}{2}[21\bar{1}]_F = [100]_\beta$[a]: SPACE GROUP $P\bar{1}$

No.	Origin of $\beta(1)$ cell[b]	Origin shift from nearest $[000]_F$ on metal atom[c]	Position of cluster centers[d]	Cluster links along $[001]_\beta$ as fluorite-type vectors
1	On metal atom or between adjacent metal atoms along $[100]_\beta$	0, 0, 0 $\frac{1}{2}$, 0, 0	$\pm\frac{1}{4}$, 0, $\frac{1}{4}$ $\pm\frac{1}{4}$, 0, $\frac{3}{4}$	$\frac{1}{2}[2\bar{1}1]$ + $\frac{1}{2}[0\bar{2}2]$
2	On metal atom or between adjacent metal atoms along $[100]_\beta$	0, 0, 0 $\frac{1}{2}$, 0, 0	$\pm\frac{1}{4}$, $-\frac{1}{6}$, $\frac{1}{4}$ $\pm\frac{1}{4}$, $\frac{1}{6}$, $\frac{3}{4}$	$\frac{1}{2}[0\bar{3}3]$ + $\frac{1}{2}[202]$
3	On metal atom or between adjacent metal atoms along $[100]_\beta$	0, 0, 0 $\frac{1}{2}$, 0, 0	$\pm\frac{1}{4}$, $-\frac{2}{6}$, $\frac{1}{4}$ $\pm\frac{1}{4}$, $\frac{2}{6}$, $\frac{3}{4}$	$\frac{1}{2}[2\bar{3}1]$ + $\frac{1}{2}[004]$
4	Halfway between adjacent metal atoms along $[100]_\beta$	0, $\frac{1}{12}$, $-\frac{1}{4}$	0, $-\frac{1}{12}$, $\frac{1}{4}$ 0, $\frac{1}{12}$, $\frac{3}{4}$	$\frac{1}{2}[1\bar{2}1]$ + $\frac{1}{2}[1\bar{1}2]$
5	Halfway between adjacent metal atoms along $[100]_\beta$	0, $\frac{1}{12}$, $-\frac{1}{4}$	$+\frac{1}{2}$, $-\frac{3}{12}$, $\frac{1}{4}$ $+\frac{1}{2}$, $\frac{3}{12}$, $\frac{3}{4}$	$\frac{1}{2}[1\bar{3}0]$ + $\frac{1}{2}[103]$
6	Halfway between adjacent metal atoms along $[100]_\beta$	$\frac{3}{4}$, 0, $-\frac{1}{8}$	$\frac{9}{24}$, $-\frac{1}{6}$, $\frac{1}{8}$ $-\frac{9}{24}$, $\frac{1}{6}$, $\frac{7}{8}$	$\frac{1}{2}[0\bar{2}0]$ + $\frac{1}{2}[2\bar{1}3]$

[a] In all cases a_β makes an angle of 61.87° with the vacancy pairs, which lie along $\frac{1}{2}[111]_F$.
[b] Relative to fluorite cations: see Fig. 1.
[c] These shifts are expressed in β-cell coordinates: e.g., see Figs. 7 and 1.
[d] Expressed as β-cell coordinates.

our preferred model is the one shown in Fig. 9, and Fig. 10a now shows the stereographic view of the cluster linkage along $[010]_\beta$ for this model. The cluster linkages along $[001]_\beta$ are of two kinds, although both are of the $\frac{1}{2}\langle 21\bar{1}\rangle_F$ type (i.e., $\frac{1}{2}[1\bar{1}2]_F + \frac{1}{2}[1\bar{2}1]_F = \frac{1}{2}[2\bar{3}3]_F$); the first makes an angle of 61.87° and the second of 90.0° with the vacancy pair axis. The former has already been shown in Fig. 5b; it is the c-axis of all the odd-numbered homologues, 7, 9, and 11. Figure 10b shows the latter linkage.

Experimental Part

The intermediate $\beta(1)$ phase $Pr_{24}O_{44}$ was prepared from a 99.999% pure oxide from Research Chemicals Inc. This oxide, purchased nominally as "Pr_6O_{11}," was heated at 1000°C in a platinum dish for 24 h to remove absorbed H_2O and CO_2, cooled to 200°C, and placed in a desiccator. The dry decarbonated product was annealed at 350 Torr oxygen pressure for 2 days at 400°C then sealed in a quartz tube. An X-ray powder diffraction pattern confirmed that the product was the $\beta(1)$ phase. A sample of this carefully-prepared material was crushed, suspended in ethanol, and supported on a holey carbon film on a microscope grid. Electron micrographs were taken with a JEOL 4000EX high-resolution electron microscope operated at 400 kV. The images were recorded at optimum defocus using a

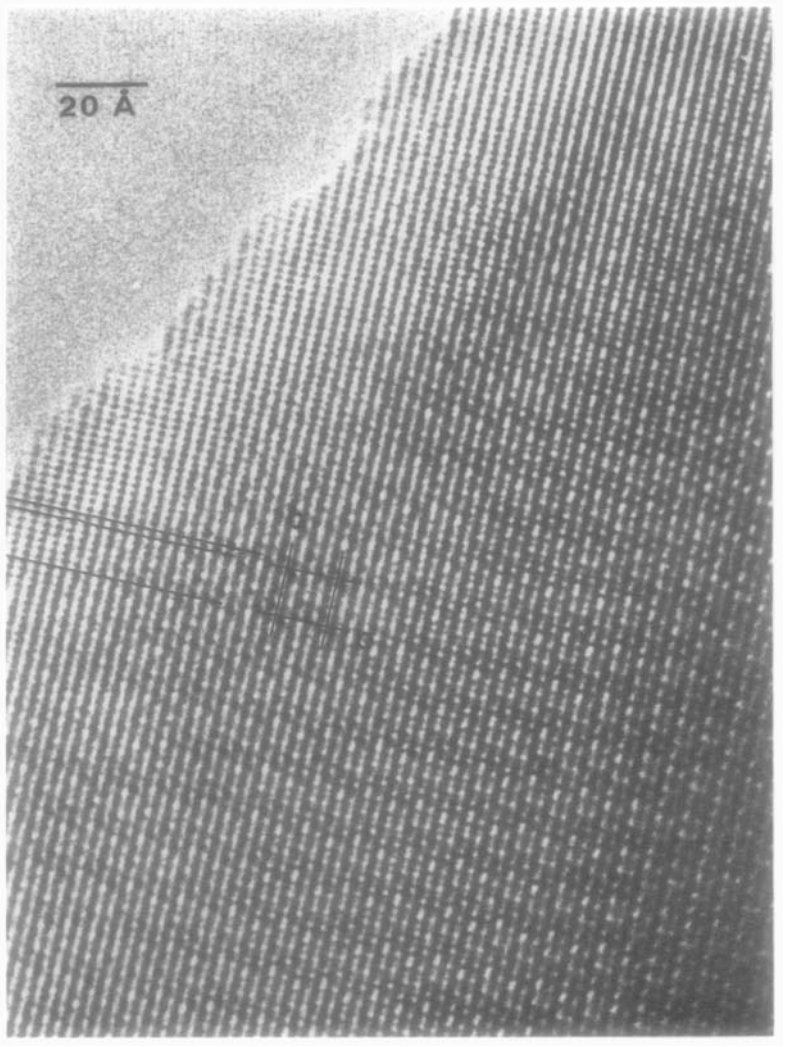

FIG. 8. HREM image of $Pr_{24}O_{44}$. The cell is shown down the $[100]_\beta$ direction and the two arrows mark the center of the two defect clusters.

current density of about 5 A/cm^2. The thin crystal was oriented down the $[2\bar{1}\bar{1}]$ fluorite vector, which is down the a-axis of the $\beta(1)$ cell. Optical diffractogram analysis was used to obtain Fourier transforms of the periodicities present in selected regions of the micrograph.

For comparison, images for various models have been calculated using the ASU Multislice program (*14*). The following parameters have been used:

Wavelength (400 kV)	0.016439 Å
No. of beams used	400
Slice thickness	6.687 Å
Objective aperture radius	0.6 Å^{-1}
Sum of multisliced beam intensities	0.9984

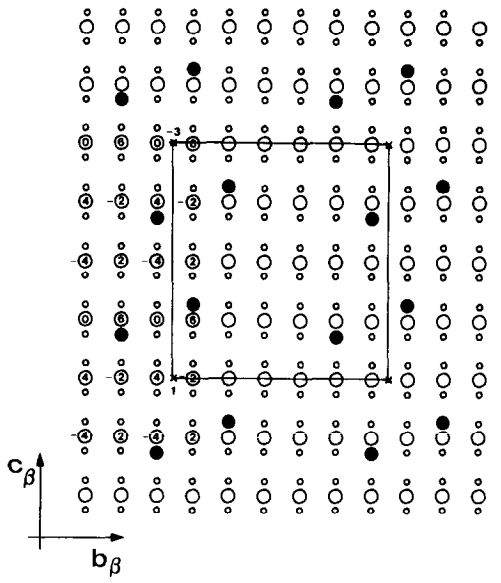

FIG. 9. An idealized projection down $[100]_\beta = \frac{1}{2}[21\bar{1}]_F$ of model 4 (Table I) for the $P\bar{1}$ structure of $Pr_{24}O_{44}$. In this model the vacancy pair axis is at 61.87° to the projection axis.

Spherical aberration	1.0 mm
Semiangle of beam convergence	1.6 mrad
Half-width of depth of focus, Gaussian	50 Å
Half-width of vibrations, Gaussian	0.8 Å
Slope of the contrast curve	1.0.

In making these calculations, the fluorite-cell coordinates of the ideal M_7O_{30} cluster were generated, with the origin on the central, 6-coordinated metal atom. These coordinates were then transformed to give coordinates in the idealized Pr_7O_{12} cell. The relationship of this cell to the fluorite cell has already been presented. Next, the fluorite positions were exchanged for those determined in the actual structure of Pr_7O_{12} (*4*), and these coordinates were finally transformed to relate to the $\beta(1)$ cell, using the relationship

$$a_\beta = a_7,$$

TABLE II
MODEL 4 IN $P\bar{1}$

Atoms	x	y	z
Pr 1	0.0000	0.0830	0.7500
Pr 2	0.9930	0.4340	0.7490
Pr3	0.5260	0.2570	0.7460
Pr 4	0.2640	0.2540	0.0150
Pr 5	0.4740	0.9100	0.7530
Pr 6	0.7360	0.9120	0.4840
Pr 7	0.0070	0.7330	0.7500
Pr 8	0.7500	0.0833	0.0000
Pr 9	0.7500	0.4167	0.0000
Pr 10	0.7500	0.2500	0.5000
Pr 11	0.2500	0.4167	0.5000
Pr 12	0.5000	0.4167	0.2500
0 1	0.8570	0.2510	0.7040
0 2	0.5625	0.4167	0.4375
0 3	0.6810	0.4360	0.8140
0 4	0.0690	0.3970	0.9350
0 5	0.8940	0.4150	0.5450
0 6	0.8135	0.5900	0.6720
0 7	0.2840	0.4060	0.6910
0 8	0.1865	0.5765	0.8270
0 9	0.5430	0.2440	0.9210
0 10	0.4650	0.4260	0.0580
0 11	0.0820	0.1020	0.9230
0 12	0.9060	0.2390	0.0610
0 13	0.5395	0.9090	0.9315
0 14	0.2905	0.2560	0.1960
0 15	0.2970	0.1050	0.7000
0 16	0.4650	0.2590	0.5580
0 17	0.7020	0.0610	0.7990
0 18	0.1430	0.9160	0.7950
0 19	0.3190	0.7310	0.6850
0 20	0.9310	0.7700	0.5640
0 21	0.5435	0.0770	0.4215
0 22	0.9180	0.0630	0.5765

$$b_\beta = 0.4286\, a_7 + 1.7143\, b_7 + 0.8571\, c_7,$$

$$c_\beta = -0.1428\, a_7 - 0.5714\, b_7 + 1.7148\, c_7.$$

For model 4, with $P\bar{1}$ symmetry, the complete set of atomic coordinates was calculated, including the origin shifts, which are shown in Table II.

Discussion of the Microscopical Results

The contrast in the HREM image, taken at optimum defocus (Scherzer defocus), of

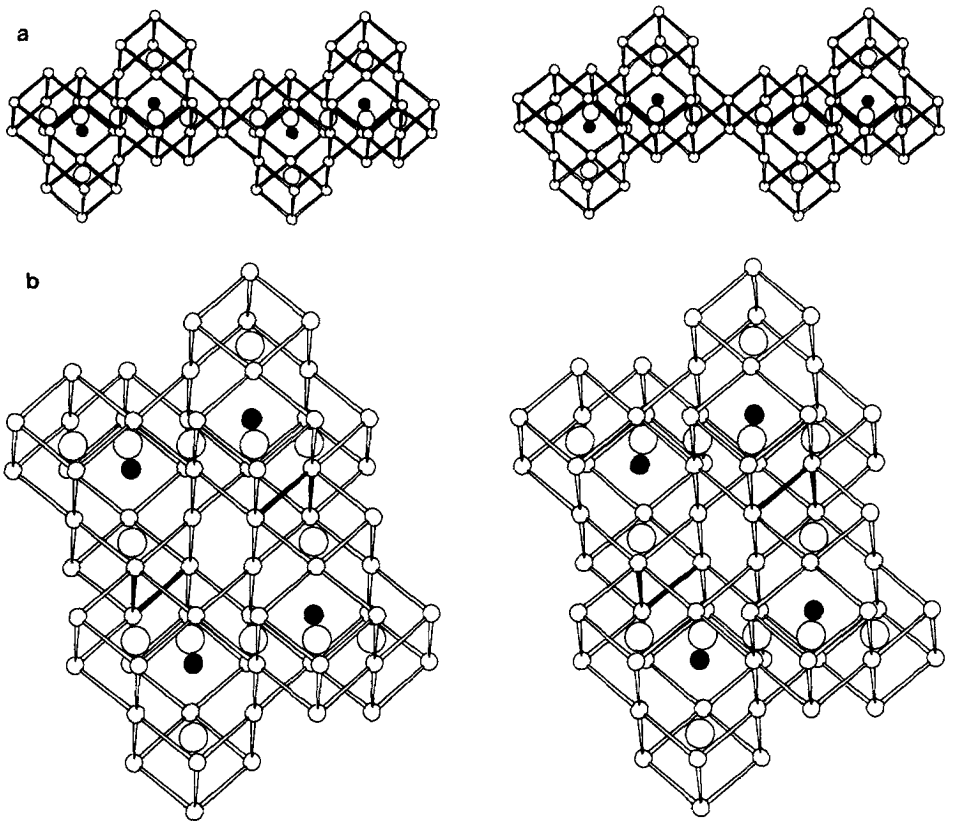

FIG. 10. The proposed structure of $Pr_{24}O_{44}$: (a) A stereoscopic view along $[100]_\beta = \frac{1}{2}[21\bar{1}]_F$ of cluster linkage along $[010]_\beta = \frac{1}{2}[033]_F$. (b) A stereoscopic view along $[100]_\beta = \frac{1}{2}[21\bar{1}]_F$ of the second type of cluster linkage along $[001]_\beta = \frac{1}{2}[1\bar{2}1]_F$ (the first is shown in Fig. 5b). The cell origin (see Fig. 7) is marked by a dot. Filled small circles indicate vacancies, cluster centers are between vacancies, and cluster junctions are highlighted.

a properly oriented crystal thin enough to approximate a phase object may be interpreted directly in terms of a local projected structure of the crystal (*15*). In order to visualize superstructures, thicker crystals are necessary and the kinematical relationship holds only for certain beams. These beams are almost in phase and have amplitudes proportional to their structure factors (*16, 17*). The behavior of the latter beams against those from the fluorite substructure has been studied.

The superstructure of $Pr_{24}O_{44}$ is caused by an oxygen-deficient sublattice that is responsible for small displacements in the metal atom positions (approximately 0.2 Å) in the cation f.c.c. arrangement. The intensity of superstructure beams depends both on the strong scattering from the slightly shifted Pr atoms and the lighter scattering from the larger distortion of the oxygen atoms. In Figs. 11a–11c a through-focus series of a crystal of $Pr_{24}O_{44}$ is shown. The images were taken down the $[100]_\beta$ direction of the unit cell which is the $[21\bar{1}]_F$ direction with respect to the fluorite subcell.

Because of the dynamical scattering of electrons a variance in beam intensities with crystal thickness and focus occurs. These intensity–thickness curves have been calcu-

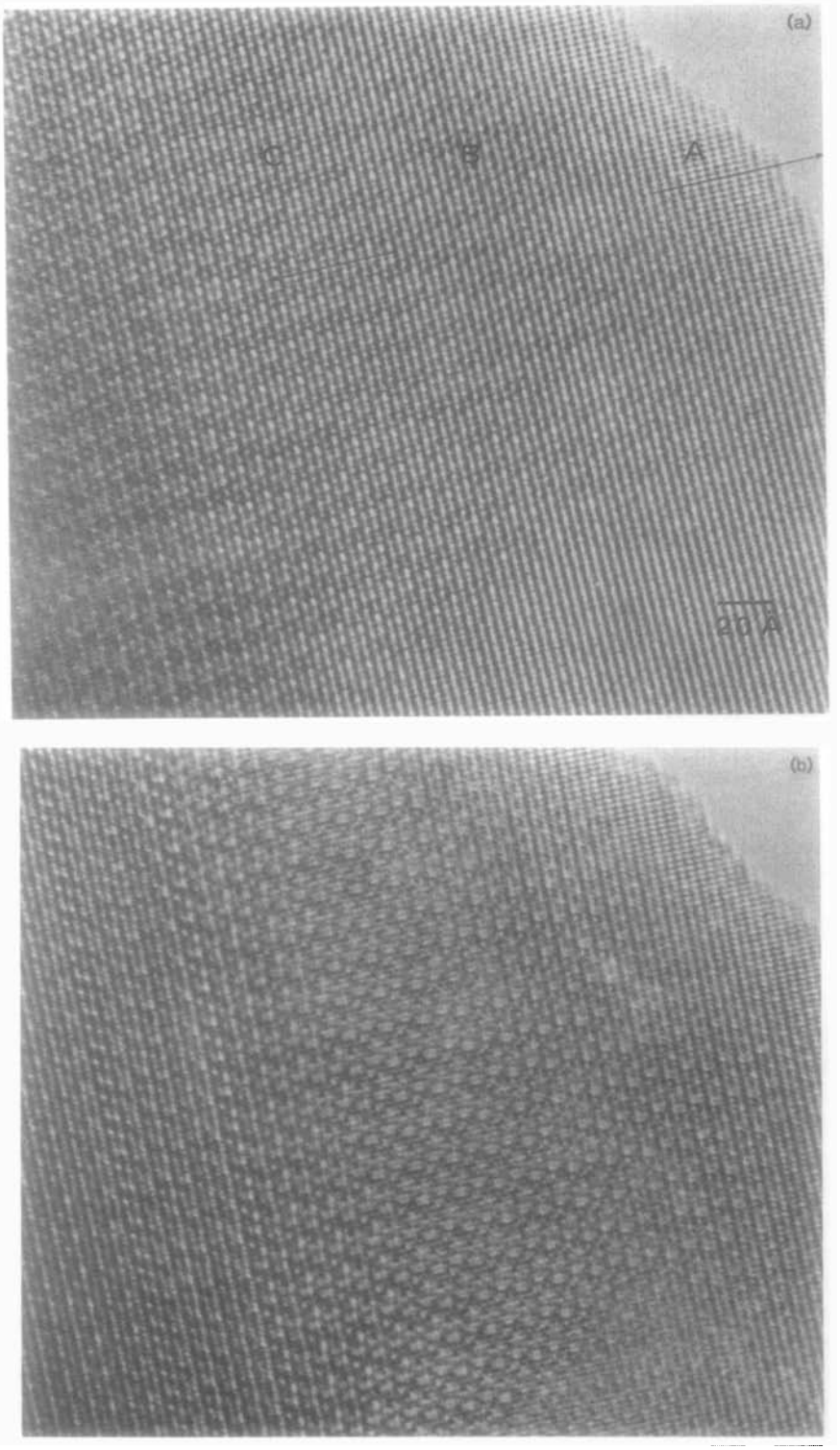
(a)
C
B
A
20 Å
(b)

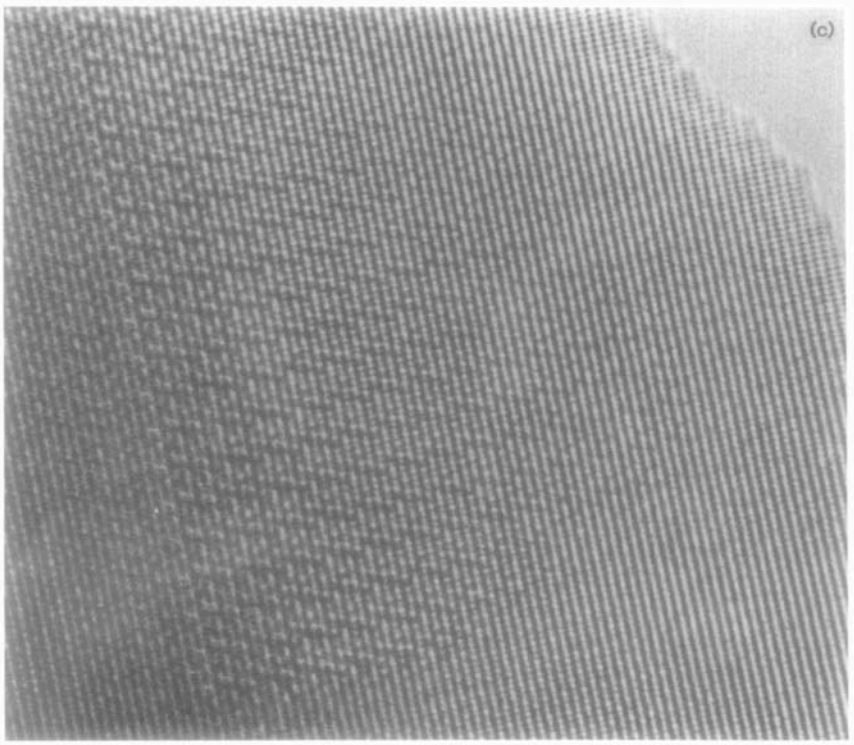

FIG. 11. A through-focus series of images of $Pr_{24}O_{44}$. All images have the same magnification and are (a) close to the Scherzer defocus and (b) 320 and (c) 640 Å underfocussed.

lated and are shown in Fig. 12. The Pendellösung plots for the zero-beam and the five strongest fluorite reflections reach a minimum at a crystal thickness of about 140 Å. Therefore, images taken at a thickness of about 140 Å should depend much more on the distortions in the oxygen sublattice than on distortions in the metal-atom sublattice. In image 11a this area occurs between the arrows. In area A the fluorite fringes are dominant and the superstructure is not visible. Area B, the area of the first thickness fringe, shows the absence of the $[200]_F$ fringes as expected. With increasing thickness the influence of the fluorite substructure becomes dominant again and the $[200]_F$ fringes reappear (C). This matching of the image with intensity–thickness curves gives a good calibration for the crystal thickness and for the image match for the different models. Calculated images (Fig. 13) show an agreement in the contrast only for model 4: the interpretation assumes that black spots correspond to the vacancies in the structure. This is the basis for our selection of model 4 (Table I), with the space group $P\bar{1}$, as the likely structure for the $\beta(1)$ phase. However, many uncertainties remain, and these will only be resolved when a full, single-crystal structure determination and refinement by total profile neutron powder diffraction analysis can be effected.

Acknowledgments

This work was supported by NSF Grant DMR-8516381 and used facilities of the National Center for High-Resolution Electron Microscopy supported by Grant DMR 8306501 within the Center for Solid State

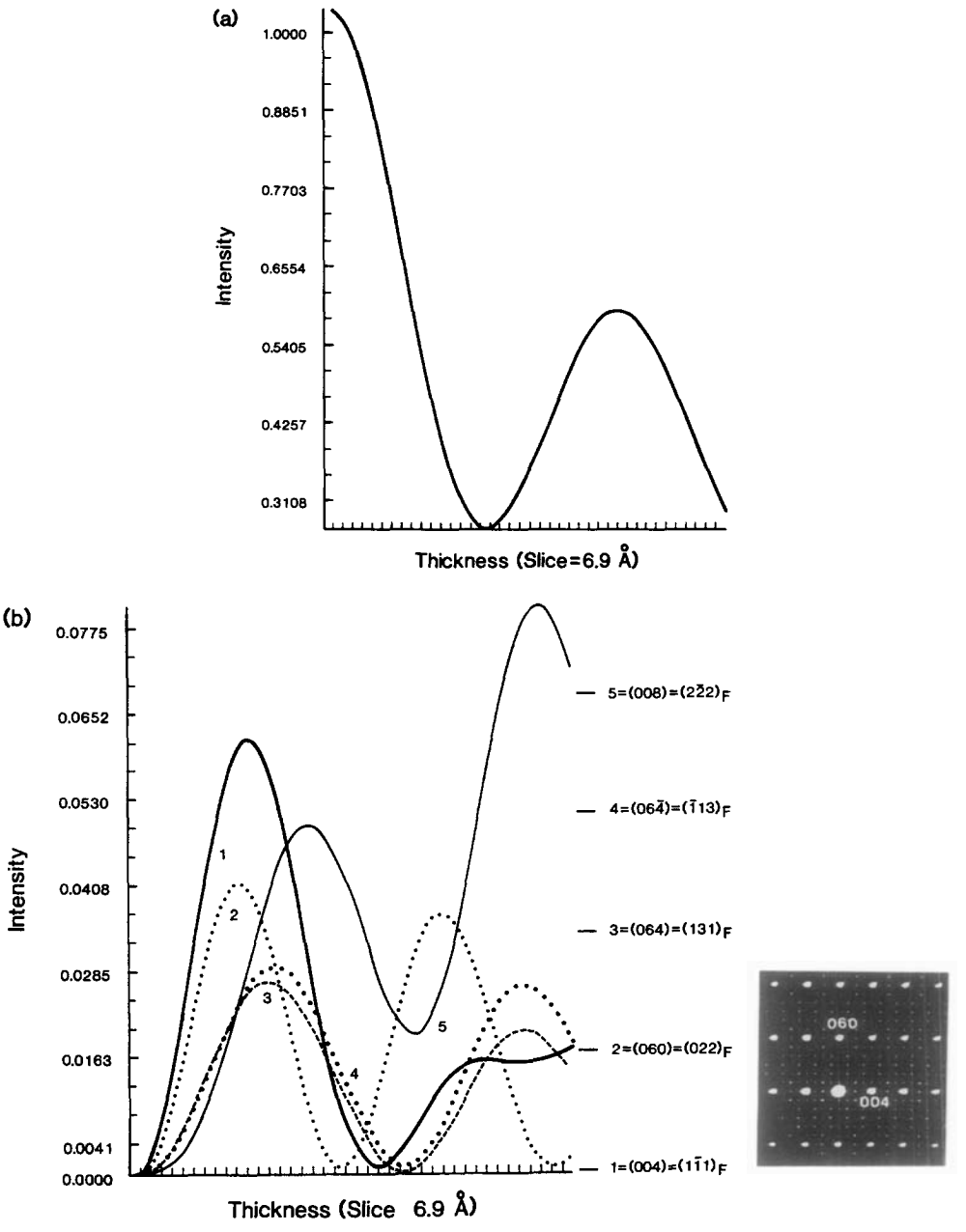

FIG. 12. The intensity–thickness plots for $Pr_{24}O_{44}$ in $P\bar{1}$: (a) The zero-beam. (b) The five strongest fluorite beams showing a common minimum at about 140 Å.

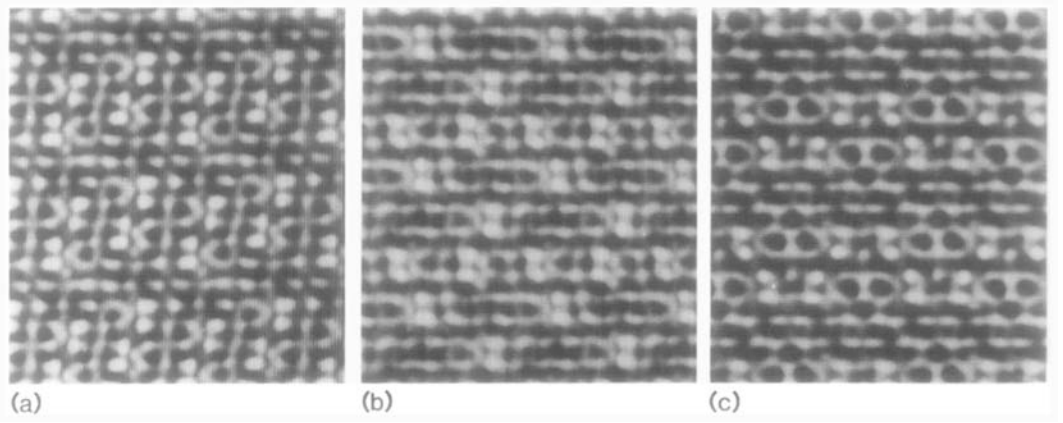

FIG. 13. The calculated image for model 4 (Table I, $P\bar{1}$) at a thickness of 140 Å and a defocus of 580 Å is shown.

Science at Arizona State University. The assistance of D. J. Smith with the JEOL 4000EX microscope is greatly appreciated.

References

1. B. G. HYDE, D. J. M. BEVAN, AND L. EYRING, *Phil. Trans. R. Soc. London Series A*, Vol. **259** (1106), 583–614 (1966).
2. P. KUNZMANN AND L. EYRING, *J. Solid State Chem.* **14,** 229 (1975).
3. N. C. BAENZIGER, H. A. EICK, H. S. SCHULDT, AND L. EYRING, *J. Amer. Chem. Soc.* **83,** 2219 (1961).
4. R. B. VON DREELE, L. EYRING, A. L. BOWMANN, AND J. L. YARNELL, *Acta Crystallogr.* **B31,** 971 (1975).
5. B. G. HYDE AND L. EYRING, *in* "Rare Earth Research III" (L. Eyring, Ed.), p. 1023, Gordon and Breach, New York (1965).
6. M. R. THORNBER, D. J. M. BEVAN, AND J. GRAHAM, *Acta Crystallogr.* **B24,** 1183 (1968).
7. S. F. BARTRAM, *Inorg. Chem.* **5,** 749 (1966).
8. JERZY KOCINSKY, "Theory of Symmetry Changes at Continuous Phase Transitions, Elsevier, Amsterdam/Oxford/New York (1983).
9. J. D. BERNAL, AND A. L. MACKAY, *Tschermaks Mineral. Petrogr. Mitt.* **10,** 3 (1965).
10. C. BOULESTEIX AND L. EYRING, *J. Solid State Chem.* **66,** 125 (1987).
11. J. O. SAWYER, B. G. HYDE, AND L. EYRING, *Bull. Soc. Chim. Fr.,* 1190–1199 (1965).
12. H. ROSSELL, private communications.
13. E. SUMMERVILLE, R. T. TUENGE, AND L. EYRING, *J. Solid State Chem.* **24,** 21 (1978).
14. M. A. O'KEEFE, ASU Multislice Program.
15. D. SHINDO, *Acta Crystallogr.* **A38,** 310 (1982).
16. R. GUAN, H. HASHIMOTO, AND K. H. KUO, *Ultramicroscopy* **20,** 195 (1986).
17. J. M. COWLEY AND S. IIJIMA, *Z. Naturforsch.* **27a,** 445 (1972).